NANO · MICRO small
www.small-journal.com

Bidirectional Inhibiting Interfacial Ion Migration in the Inorganic Hole Transport Layer for Perovskite Light-Emitting Diodes

Lunyao Pan, Xiankan Zeng, Yuanxiao Qu, Maolin Mu, Shiyu Yang, Yongjian Chen, Chenglong Li, Linzhu Dai, Li Tao, Hongqiang Xin, Wen Li, and Weiqing Yang**

Cu_2ZnSnS_4 (CZTS) is strong candidate for hole transport in perovskite light emitting diodes (PeLEDs) due to their cost-effectiveness, deep highest occupied molecular orbital (HOMO), and high hole mobility. However, its inherent polymetallic ions usually deteriorate the quality of the perovskite emission layer (EML) affecting device performance. In this study, a bidirectional anchoring strategy is proposed by adding 15-crown-5 ether (15C5) into CZTS hole transport layer (HTL) to suppress the reaction between HTL and EML. The 15C5 molecule interacts with Cu^+, Zn^{2+} and Sn^{2+} cations forming host–guest complexes to impede their migration, which is elucidated by density functional theory calculations. Additionally, 15C5 can neutralize lead (Pb) defects by the abundant oxygen (O) and high electronegative cavities to reduce the nonradiative recombination of $FAPbBr_3$ film. This bidirectional anchoring strategy effectively improves hole charge transport efficiency and suppresses nonradiative recombination at the HTL/EML interface. As a result, the optimized PeLEDs present a 3.5 times peak external quantum efficiency (EQE) from 3.12% to 11.08% and the maximum luminance (L_{max}) increased from 24495 to 50584 cd m^{-2}. These findings offer innovative insights into addressing the metal ion migration issue commonly observed in inorganic HTLs.

1. Introduction

Perovskite light-emitting diodes (PeLEDs) have garnered substantial attention in recent years owing to their high color purity, exceptional charge transport properties, and cost-effective manufacturing.[1–5] However, the hole transport layer (HTL) in PeLEDs is always unsatisfactory, which leads to deterioration of the operational stability and the device efficiency, inhibiting their large-scale commercial manufacturing. Traditional organic HTL materials usually exhibit inherent drawbacks, including limited stability, expensive material component and incompatible interface with the perovskite layer.[6–8] To overcome these challenges, it is imperative to investigate inorganic HTL materials with superior properties, including high thermal stability, chemical robustness, low cost and adjustable electronic structures. These inorganic HTL can afford balanced carrier injection with matched energy band alignment and enhanced operational stability, which is beneficial for the commercial applications of PeLEDs.[9–13]

The inorganic HTL contains metal ions, and some types of metal ions will cause the fluorescence attenuation of the perovskite emitting layer (EML). Metal ions situated at the periphery of the inorganic HTL lattice tend to detach easily and diffuse into the upper perovskite EML during thermal annealing, thereby damaging the structural integrity of the perovskite and further diminishing the electroluminescence performance of PeLEDs.[12,14,15] Therefore, the problem of addressing ion migration has become a primary goal in the widespread application of inorganic HTL in PeLEDs. Currently, most research focus on inserting interlayers at the HTL/EML interface and modifying the EML to inhibit ion migration. These approaches aim to protect the lattice integrity of perovskites and suppress

L. Pan, X. Zeng, Y. Qu, M. Mu, S. Yang, Y. Chen, C. Li, W. Li, W. Yang
Key Laboratory of Advanced Technologies of Materials (Ministry of Education)
School of Materials Science and Engineering
Southwest Jiaotong University
Chengdu 610031, P. R. China
E-mail: liwen3337@swjtu.edu.cn; wqyang@swjtu.edu.cn

L. Dai
School of Chemistry and Chemical Engineering
Southwest University
Chongqing 400715, P. R. China

L. Tao
School of Optoelectronic Engineering
Chengdu University of Information Technology
Chengdu 610225, P. R. China

H. Xin
School of New Energy and Power Engineering
Lanzhou Jiaotong University
Lanzhou 730070, P. R. China

W. Yang
Research Institute of Frontier Science
Southwest Jiaotong University
Chengdu 610031, P. R. China

The ORCID identification number(s) for the author(s) of this article can be found under https://doi.org/10.1002/smll.202405528

DOI: 10.1002/smll.202405528

interface quenching.[16–19] Nevertheless, few strategies are reported to inhibit ion migration based on the design of inorganic HTL materials. The inorganic compound Cu_2ZnSnS_4 (CZTS) as a typical polymetallic ion sulfide, has increasingly been utilized as inorganic HTL materials due to its deep highest occupied molecular orbital (HOMO), high hole mobility and cost-effective production.[20,21] However, the use of CZTS HTL can lead to fluorescence quenching of perovskite EML due to metal ions migration. In order to inhibit this undesirable migration at the HTL/EML interface, an effective solution is to incorporate passivators into the HTL to form strong binding with metal ions.[22,23] Crown ether, a promising passivation material, can form host–guest complexes with metal ions due to its electronegative cavities.[24–26] Moreover, the abundance of oxygen (O) atoms in crown ether enables effective neutralization of these positive defects in perovskite materials.[27] Therefore, crown ether is expected to address the issue of metal ions migration between the HTL and EML in PeLEDs.

Here, we incorporated the organic bidirectional anchoring molecule 15-crown-ether (15C5) into the inorganic material CZTS to create a novel HTL (15C5 CZTS). The combination of crown ether and Cu^+ effectively suppresses ion migration in the CZTS HTL, thereby maintaining the integrity of the EML. Additionally, crown ethers passivate the perovskite surface and reduce annihilation traps. This bidirectional anchoring enhances carrier dynamics, leading to improved charge transport and efficient radiative recombination. As a result, the peak external quantum efficiency (EQE) increased from 3.12% to 11.08%, maximum luminance (L_{max}) increased from 24495 to 50584 cd m^{-2}, and current efficiency (CE) increased from 15.03 to 50.42 cd A^{-1}, corresponding to improvements of 355%, 207%, and 335%, respectively. This work achieves the highest performance record for CZTS-based PeLEDs, providing novel insights into the common ion migration issue that hinders inorganic HTLs, and offering guidance for further development towards efficient and stable inorganic HTLs.

2. Results and Discussion

To understand the mechanism of crown ether complexation and passivation, density function simulation (DFT) calculations were performed based on two crown ethers, 15-crown-5 ether (15C5) and 12-crown-4 ether (12C4). Calculated binding energy (E_b) between the crown ether and three metal ions (Cu^+, Zn^{2+}, and Sn^{2+}) in CZTS follow the order: 15C5@Cu^+ (15.167 eV) > 12C4@Cu^+ (12.797 eV), 15C5@Zn^{2+} (14.982 eV) > 12C4@Zn^{2+} (13.445 eV), and 15C5@Sn^{2+} (8.592 eV) > 12C4@Sn^{2+} (7.681 eV) (**Figure 1**a,b). Figure S1 (Supporting Information) visually demonstrates the quenching effect of three metal ions on $FAPbBr_3$ after thermal annealing diffusion (Cu^+ in CuCl, Zn^{2+} in $ZnCl_2$ and Sn^{2+} in $SnCl_2$), the identical Cl^- eliminate the influence of anions. It is evident that Cu^+ markedly quenches the perovskite layer compared to Zn^{2+} and Sn^{2+}. After treated by 12C4 and 15C5, 15C5 treated sample significantly retain original fluorescence properties of perovskite EML, suggesting 15C5 coordinated with Cu^+ forms host–guest complexes through hydrogen bonding to avoid damage to perovskite.[28–30] Depending on the size of the ring structure of ether groups, the electronegative cavity of the 15C5 showed stronger complexation with target metal ions than 12C4, which is consistent with the results of theoretical calculation.

Figure 1c,d presents the equilibrium configurations of the $FAPbBr_3$ (001) and crown ether-passivated surfaces. Previous studies have reported that 15C5 can trap Pb^{2+} ion to form a stable complex, reducing interlayer diffusion and loss of Pb.[27,31–33] Additionally, Pb in perovskite interacts with O atoms possessing high electron affinity within crown ethers to suppress non-radiative traps caused by Pb vacancies.[32,34] In Figure 1c,d, and Figure S2 (Supporting Information), the E_b of 15C5 combine and Pb^{2+} cations to form the hydrogen-bonding (0.565 eV) and Pb—O strong coordination bonds (0.824 eV) in the upper perovskite are higher than of 12C4 (0.534 eV and 0.816 eV). Furthermore, Figure S3 (Supporting Information) shows that the blue shift of the perovskite film on the 15C5 treated CuCl film is significantly enhanced compared to that on 12C4 treated CuCl film, suggesting superior passivation capabilities for Pb-associated shallow defects by 15C5. In summary, theoretical results prove that 15C5 demonstrates stronger complexation with buried CZTS layer and better defect passivation for perovskite layer than 12C4 (Figure 1e). Figure 1f clearly shows the bidirectional anchoring effect of crown ether, which inhibits Cu^+ migration in HTL and passivates the Pb defects in EML, and finally obtains high quality HTL/EML interface.

Fourier transform infrared spectroscopy (FTIR) was conducted to elucidate the interaction between 15C5 and CZTS (**Figure 2**a). An additional peak of C—O—C bonds exhibited in 15C5-modified CZTS (15C5 CZTS) compared to pure CZTS (W/O CZTS), and this peak shifts slightly from 1130 to 1134 cm^{-1} compared to pure 15C5. This change indicates a compact chemical bond formation between the electronegative cavity of 15C5 and Cu^+ in CZTS, resulting in either bond contraction or an intensified vibration mode.[23,35] X-ray diffraction (XRD) patterns show that there are no additional peaks and peak shift for 15C5 treated CZTS sample, indicating that the crystal structure of CZTS remains unchanged (Figure 2b), which is consistent with the uniform Raman peaks (287 and 337 cm^{-1}) (Figure S4, Supporting Information). Furthermore, the Tauc plots and UPS spectra of CZTS simples demonstrate the negligible influence of 15C5 on the energy band structure of the CZTS HTL (Figure S5, Supporting Information). These findings suggest that 15C5 molecules are anchored to the surfaces of CZTS nanocrystals.

The inhibition of Cu^+ migration between CZTS HTL and perovskite EML was investigated by temperature-dependent photoluminescence (PL) spectra, and a comprehensive understanding of the nonradiative relaxation process and exciton–phonon coupling behavior of perovskite films can be achieved. The full width half maximum (FWHM) curves extracted from 2D temperature-dependent PL maps (Figure 2c,d) and 3D PL diagrams (Figure S6, Supporting Information) were fitted, showing excellent agreement between experimental data and the optimal fitting curve ($R^2 > 0.95$), the parameters obtained are summarized in Table S1 (Supporting Information). Furthermore, the exciton binding energy (E_B) of HTL/perovskite interface was determined by using Arrhenius equation to the PL spectra:[36,37]

$$I\ (T) = \frac{I_0}{1 + Ae^{\left[-E_B/k_B T\right)}} \quad (1)$$

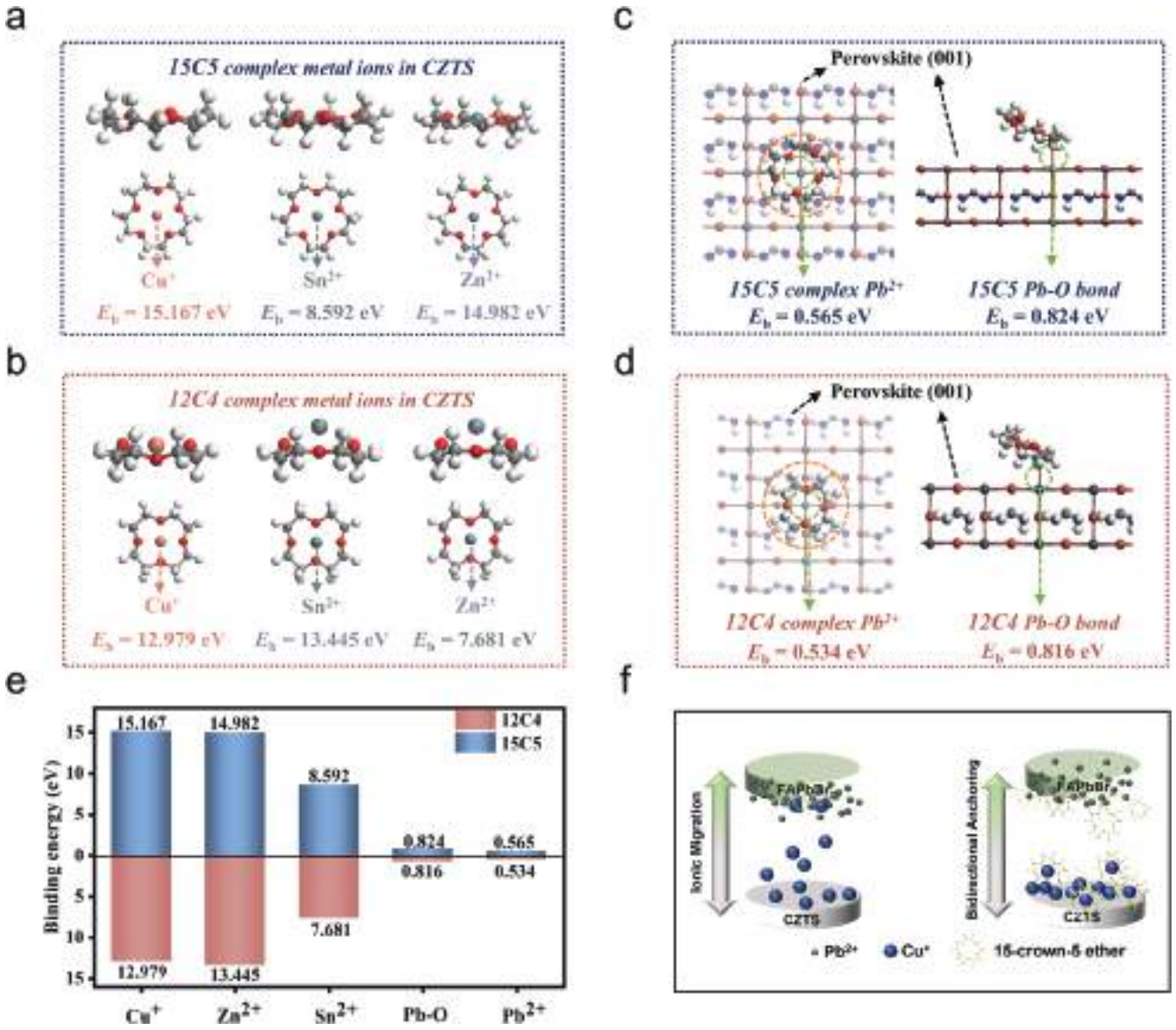

Figure 1. The optimized structure and binding energy (E_b) of a) 15-crown-5 ether and b) 12-crown-4 complexes with Cu^+, Zn^{2+}, and Sn^{2+}. The equilibrium configurations of the $FAPbBr_3$ (001) and c) 15-crown-5 ether, d) 12-crown-4 ether passivated surfaces. e) Bidirectional anchoring E_b of crown ether. f) Schematic diagram of theoretical design of 15-crown-5 ether bidirectional anchoring.

where I_0 is the PL integral strength at the temperature of T_0, A is the proportional coefficient. In general, E_B represents the energy required for the exciton to dissociate into a free carrier, and a larger E_B indicates a higher binding barrier between the exciton and the intact stable perovskite lattice.[38,39] In both W/O CZTS and 15C5 CZTS spin-coated perovskite film, E_B increases from 173.93 to 262.36 meV in Figure 2e, indicating that 15C5 treated CZTS HTL notably improves the stability of the perovskite lattice and reducing nonradiative trap centers. The exciton–phonon coupling coefficient of the HTL/perovskite interface can be extracted using the Frohlich formula, which accounts for the temperature-induced FWHM broadening:[40,41]

$$\Gamma\ (T) = \Gamma_0\ + \Gamma_{AC} + \ \Gamma_{LO} = \Gamma_{inh}\ + \gamma_{AC}T + \gamma_{LO}/[e^{E_{LO}/k_BT} - 1 \quad (2)$$

where Γ_0 is an intrinsic inhomogeneous broadening due to material composition, size, and shape. Γ_{inh} stems from optical phonon scattering, contributing to the broadening of the PL emission line. k_B is the Boltzmann constant. The γ_{AC} and γ_{LO} represent the exciton–acoustic phonon coefficient and exciton–phonon coupling coefficient, respectively. In $FAPbBr_3$ quantum dots (QDs), phonon scattering's influence can be neglected and E_{LO} denotes the phonon energy.[42,43] In $FAPbBr_3$ film obtained from W/O and 15C5 CZTS, E_{LO} decreases from 34.42 to 27.22 meV (Figure 2f and Table S1, Supporting Information). The decrease in E_{LO} indicates a reduction in exciton–phonon coupling strength and an enhancement in lattice stability, which is attributed to the complexation of 15C5 with Cu^+ ions in CZTS. This complexation effectively suppresses migration of Cu^+, thereby enhancing the stability and integrity of perovskite lattice. Similarly, the Urbach energy

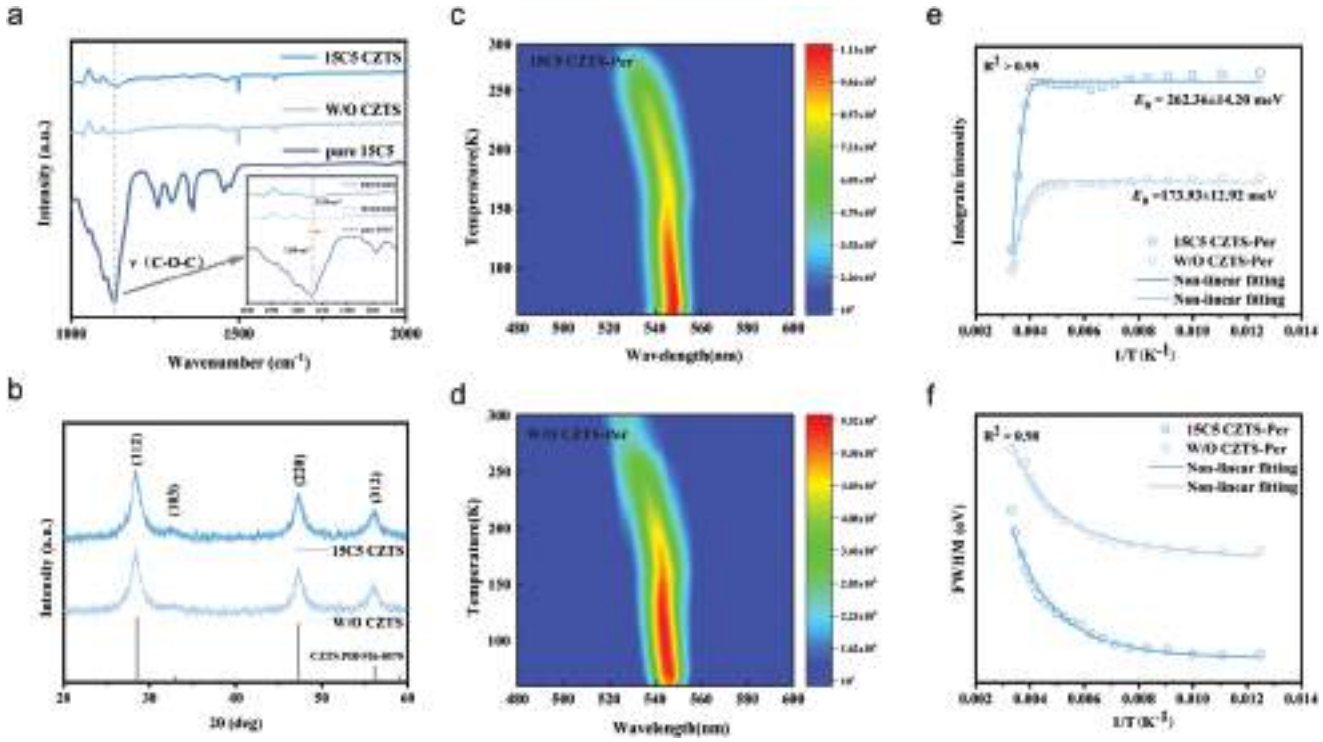

Figure 2. a) FTIR spectra of 15C5 CZTS, W/O CZTS and pure 15C5 films, b) XRD patterns of 15C5 CZTS and W/O CZTS films. c,d) 2D temperature-dependent PL spectra of the perovskite films on 15C5 CZTS and W/O CZTS. e) Integrated PL intensity as a function, h) FWHM of reciprocal temperature.

(E_u) serves as a metric for quantifying thermal and intrinsic structural disturbances and disorders in crystals, where a higher E_u indicates greater structural disorder and lattice disturbance.[44,45] The E_u decreased from 156.49 to 142.45 meV of the upper perovskite film, indicating successful enhancement in its lattice integrity through 15C5 modification of CZTS (Figure S7, Supporting Information). Figure S8 (Supporting Information) shows that XRD peak of $FAPbBr_3$ on W/O CZTS exhibits a significant shift towards a higher angle during thermal annealing, which indicates that Cu^+ (76 pm) with a smaller ionic radius than FA^+ (263 pm) might be partially incorporated into the perovskite lattice, and the lattice parameters of perovskite decrease due to the difference of thermal expansion coefficient between the buried layer inorganic HTL CZTS and the upper perovskite $FAPbBr_3$. Conversely, the significant inhibition of peak shift observed in the 15C5 CZTS sample further confirms the suppression of Cu^+ migration.[46]

Crown ethers has been found to positively affect the quality of perovskite EMLs due to the O abundance in the molecule. In order to investigate the impact of 15C5 on the morphological behavior of $FAPbBr_3$ films, atomic force microscopy (AFM) images were employed (**Figure** 3a–c). The root mean square (RMS) roughness is 3.24 nm for $FAPbBr_3$ films on 15C5 modified CZTS HTL, which is markedly lower than that on the unmodified HTL (7.44 nm). Furthermore, top-view scanning electron microscope (SEM) images demonstrate the voids and pinholes of $FAPbBr_3$ film almost vanish after treatment of CZTS with 15C5 (Figure 3d,e), the dense perovskite film could effectively suppress leakage current. Meanwhile, the optical properties of $FAPbBr_3$ films on different HTL are investigated, the photoluminescence quantum yield (PLQY) of perovskite films increased from 50.24% (pure CZTS HTL) to 77.85% (15C5 modified CZTS HTL), and high PL intensity and a slight blue shift in PL peaks indicate that the interaction between 15C5 treated CZTS and $FAPbBr_3$ (Figure 3f). The corresponding decay time increases from 14.61 to 57.22 ns (Figure 3g), confirming 15C5 plays a key role in reducing nonradiative recombination of perovskite EML.[47,48] To validate the excellent defect-passivating effect of 15C5, the PL spectra of $FAPbBr_3$ films on pure 15C5, untreated CZTS HTL, and ITO films were shown in Figure S9 (Supporting Information). Only $FAPbBr_3$ film on pure 15C5 film exhibits blue shift, indicating the interaction of 15C5 with perovskite. Passivation defects may reduce the probability of carriers being trapped by the defect states, allowing more carriers to recombine in the band gap of perovskite, resulting in a shift in the direction of the PL peak toward high energy (blue shift). This may be attributed to the formation of a host–guest complex between 15C5 and the Pb^{2+} to mitigate Pb^{2+} shedding, which is consistent with previous discussion (Figure S3, Supporting Information).[32] Space charge limited current (SCLC) was further analyzed to estimate the trap density of $FAPbBr_3$ film (Figure 3h,i). Current density–voltage (J–V) curves based untreated CZTS HTL hole-only devices (HOD) show the trap-filling limiting voltage (V_{TFL}) of 1.94 V, while V_{TFL} is 1.79 V for the CZTS-based HOD treated with 15C5. The relationship between the trap density n_t and V_{TFL} can be determined by utilizing the equation $V_{TFL} = qn_tL^2/2\epsilon\epsilon_0$,[49] where q is the elementary charge, L is the thickness of the EML layer, ϵ is the dielectric constant, and ϵ_0 represents the vacuum permittivity (Figure S10, Supporting Information). The decreased n_t (2.61×10^{18} cm^{-3}) for optimized HOD evidence that

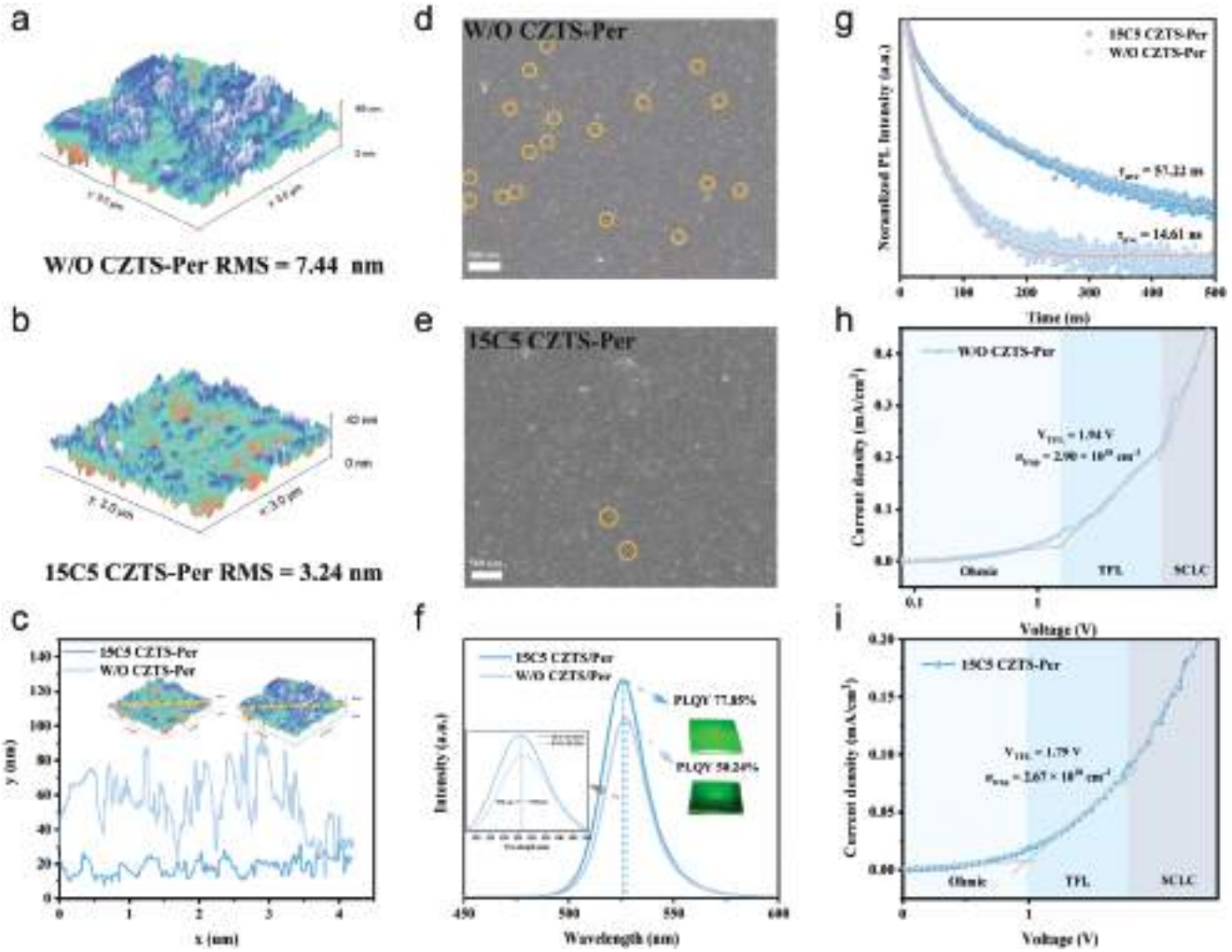

Figure 3. Defect state of perovskite film. a,b) 3D topographic AFM characterization, c) the height variations along the dotted path, d,e) top-view SEM images, f) PL spectra and PLQY, g) TRPL spectra of perovskite films on W/O CZTS and 15C5 CZTS. h,i) Current density–voltage (*J*–*V*) of W/O CZTS-based and 15C5 CZTS-based hole-only devices (HOD).

incorporating 15C5 in the buried CZTS effectively reduces defects in $FAPbBr_3$ film. Moreover, the Tauc plots and UPS spectra of perovskite films indicate defect passivation of 15C5 does not change the energy band structure of EML (Figure S11, Supporting Information). Therefore, the negatively charged cavity of 15C5 inhibits the Cu^+ migration in CZTS and a host–guest complex with Pb^{2+} through hydrogen bonding interactions anchored Pb of $FAPbBr_3$ film, thereby improving the quality of perovskite EML.

We fabricated devices with the structure of ITO/CZTS/$FAPbBr_3$/TPBi/LiF/Al and employed semiquantitative capacitance–voltage (*C*–*V*) measurements to assess interfacial carriers dynamics.[50] At low frequency of 5 KHz (**Figure 4a**), the diffusion capacitance (C_g) reflects the degree of carrier accumulation at the interface.[51,52] The 15C5 CZTS-based device exhibited lower C_g (3611 pF) than the W/O CZTS-based device (3671 pF), indicating reduced charge accumulation and enhanced charge transport efficiency in the former, which may be attributed to the weakened interfacial polarization induced by the inhibition of Cu^+ migration. Additionally, the derivative of capacitance–voltage (d*C*/d*V*) analysis revealed that the 15C5 CZTS-based device (−3.41 nF V^{-1} at 6.47 V) exhibited a more negative trend and a longer decreasing region than the W/O CZTS-based device (−2.21 nF V^{-1} at 6.39 V) (Figure 4b), suggesting enhanced carrier recombination capabilities.[53] At high frequency (f = 100 KHz), the response of defect-related carrier behavior to AC signal is weakened and the effective injection and recombination behavior of carriers are amplified at DC voltage. The 15C5 CZTS device showed increased capacitance at low voltage, indicating elevated carrier injection level (Figure S12, Supporting Information). Conversely, the W/O CZTS device demonstrated a more negative d*C*/d*V* value at high voltage, implying enhanced charge recombination efficiency in the 15C5 CZTS-based device.

Considering that capacitive and resistive elements are directly related to charge injection and recombination in semiconductor devices, impedance and reactance spectroscopy featuring multiscale electrical response was used to investigate charge transport

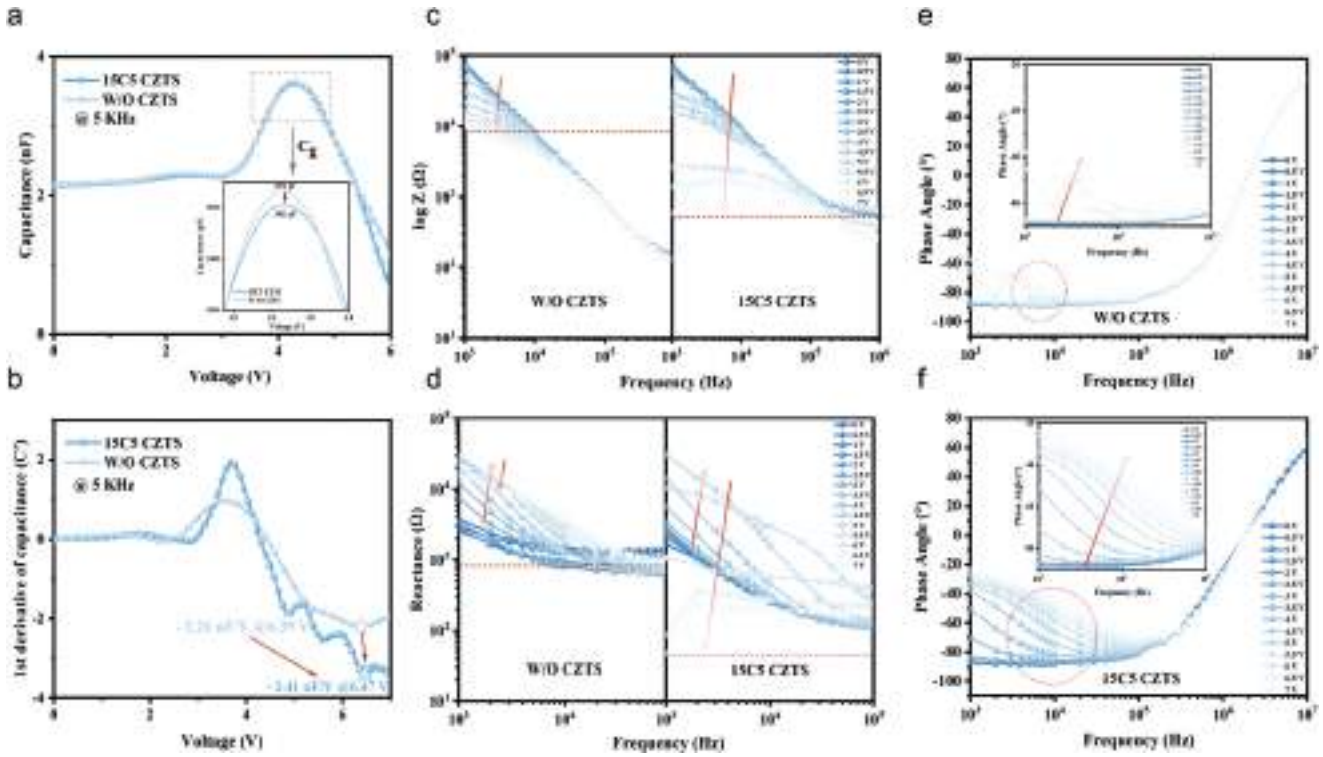

Figure 4. Carrier behavior in PeLEDs. a) Low-frequency capacitance–voltage (*C–V*) plots ($f = 5$ KHz), b) d*C*/d*V*–*V* curves, c) impedance, d) reactance and e,f) phase angle of PeLEDs.

kinetics and relaxation process in PeLEDs. Impedance measurements revealed a more pronounced decrease in impedance of the 15C5 CZTS-based device (from 7.6×10^4 Ω at 0 V to 560 Ω at 7 V at 10^3 Hz) compared to the W/O-based device (from 7.6×10^4 Ω at 0 V to 8.7×10^3 Ω at 7 V at 10^3 Hz) (Figure 4c), indicating enhanced radiative recombination at the HTL/perovskite interface.[54,55] Moreover, the analysis of reactance indicated a more dramatic decrease in the 15C5 CZTS device. Specifically, the reactance increased from 1.64×10^3 Ω at 0 V to 3.07×10^4 Ω at 4.5 V, and further decreased to 45 Ω at 7 V. In contrast, the W/O CZTS device exhibited increase from 2.43×10^3 Ω at 0 V to 3.01×10^4 Ω at 4.5 V, reaching 1.45×10^4 Ω at 7 V (Figure 4d). These results suggest reduced energy consumption in carrier transport and recombination processes of 15C5 CZTS device, verifying the passivation of perovskite defects and an improvement in lattice integrity.[56,57] Electrical impedance spectroscopy (EIS) measurements confirmed the carrier behavior in CZTS-based PeLEDs over the frequency range of 0.1 Hz to 1 MHz (Figure S13, Supporting Information). The recombination resistance of PeLEDs was determined by fitting an equivalent circuit diagram derived from the Nyquist curve. The 15C5 CZTS device exhibited higher recombination resistance (R_{rec} = 489 Ω) compared to the W/O CZTS device (R_{rec} = 460 Ω), indicating increased charge radiative recombination.[32,55,58] The phase angle in the impedance spectra represents the phase difference between the real part (resistance) and the imaginary part (reactance, including capacitive and inductive components) of the impedance in an AC circuit, therefore, the voltage-dependent alternating dominant behavior of the resistance and capacitance in the system leads to irregular changes in the phase angle.[59] Figures 4e,f and S14 (Supporting Information) show more significant phase angle variations in the 15C5 CZTS device compared to the W/O CZTS device with increasing voltage. This suggests that the 15C5 CZTS device possesses higher anti-disturbance capability and lower trap response to electric fields, implying improved carrier recombination efficiency.

Figure 5a intuitively illustrates the bidirectional anchoring mechanism of 15C5-modified CZTS as the HTL, based on the photophysical characteristics and interface carrier behaviors. On the one hand, 15C5 prevents the migration of Cu^+ migration between CZTS HTL and $FAPbBr_3$ EML. On the other hand, 15C5 can passivate the Pb defects. These improvements lead to increased carrier losses and hindered charge transport. We then compared the performance of 15C5 CZTS and W/O CZTS HTL-based PeLEDs, and the energy level diagram of device is illustrated in Figure S15 (Supporting Information). The current density–luminance–voltage (*J–L–V*) curves reveal significantly lower leakage current in the optimized 15C5 CZTS device (Figure 5b). Under high voltage conditions, the 15C5 CZTS-based device demonstrates higher current density than W/O CZTS-based device and the turn-on voltage (V_{on}) decreased to 3.0 V (W/O device, 3.2 V), and the V_{on} represents the threshold voltage applied to the carrier for effective radiative recombination, which verified that the addition of 15C5 facilitates the defect suppression and carrier radiative recombination. These improvements are consistent with the increase in maximum luminance (L_{max}) from 24495 to 50584 cd m^{-2}, current efficiency (CE) from 15.03 to 50.42 cd A^{-1}, and peak EQE from 3.12%

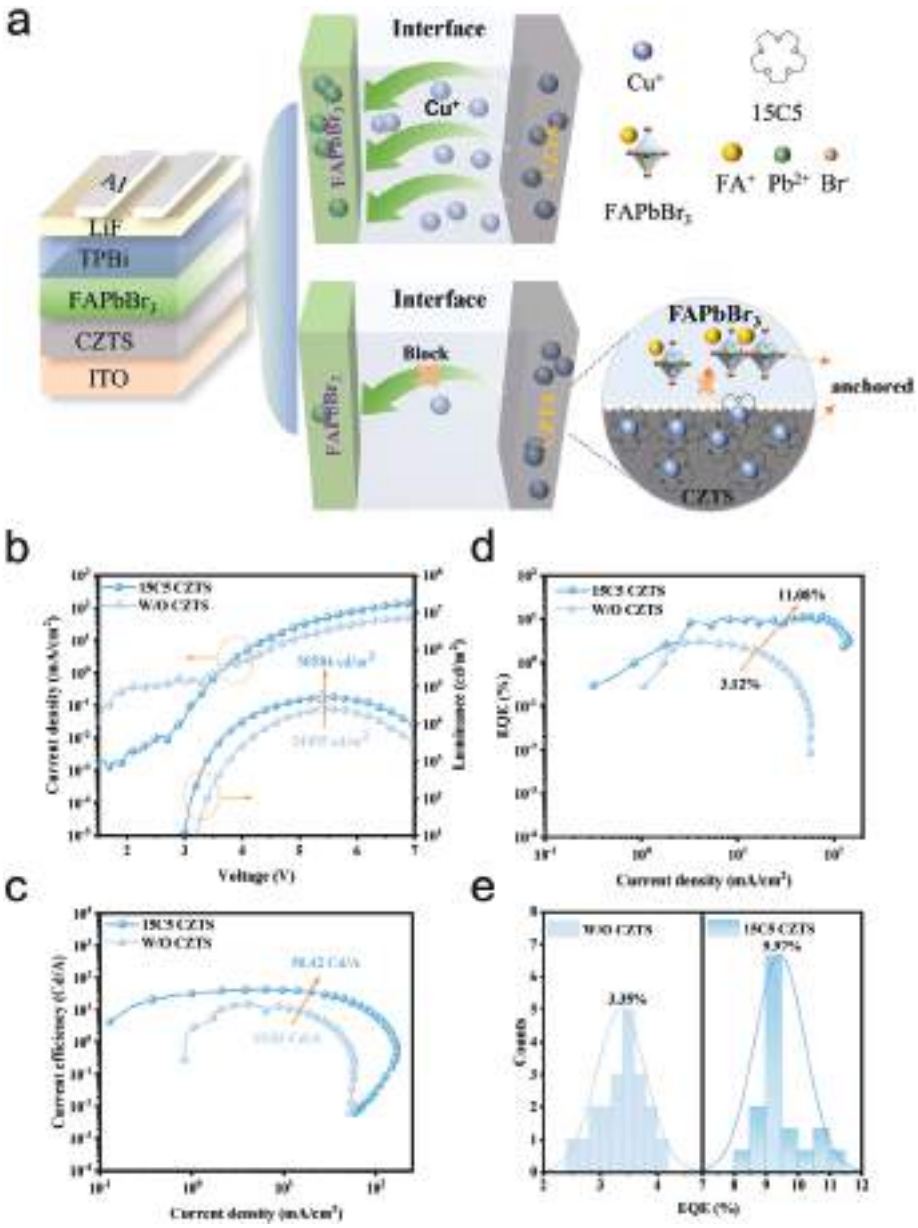

Figure 5. Device structure and EL performance characteristics of 15C5 CZTS-based and W/O CZTS-based PeLEDs. a) Schematic diagram of 15C5 bidirectional anchoring, b) current density–luminance–voltage (*J*–*L*–*V*) curves, c) current efficiency–current density (CE–*J*) curves, d) EQE–CE curves, e) histograms of peak EQE of 15C5 CZTS-based and W/O CZTS-based PeLEDs.

to 11.08% (Figure 5c,d). In contrast, the performance improvement in the 12C4-modified CZTS device is comparatively modest (Figure S16, Supporting Information), which is consistent with previous DFT calculations (Figure 1a–d). Multiple batches of PeLEDs were fabricated to verify the reproducibility and superior performance of 15C5 CZTS-based device. On average, 15C5 CZTS-based PeLEDs achieved a remarkable EQE of 9.97%, significantly surpassing the 3.35% average EQE of W/O CZTS-based PeLEDs (Figure 5e). Meanwhile, the half lifetime (T_{50}) represents the time required for the luminance to decay from 100 to 50 cd m^{-2} under constant voltage of devices. It can be calculated using the formula $L_0^n\ T_{50} = a$, where L_0 is the initial luminance, n is the exponential parameter characterizing the device and a is a constant. In comparison with W/O CZTS (5.21 min) and PEDOT:PSS-based PeLEDs (2.26 min), the T_{50} of 15C5 CZTS device is increased to 10.42 min, which can be attributed to the inherent strong stability of CZTS itself and the advantageous bidirectional anchoring of 15C5 (Figure S17, Supporting Information). Additionally, the HTL with 15C5-modified NiO_x (Device structure: ITO/NiO/$FAPbBr_3$/TPBi/LiF/Al) further enhanced performance of PeLEDs, highlighting the potential of crown ether to inhibit ion migration in inorganic HTLs and passivate defects of perovskite film (Figure S18, Supporting Information).

3. Conclusions

In summary, we successfully improved the performance of CZTS-based PeLEDs by employing a bidirectional anchoring strategy through the incorporation of 15C5 into the HTL. 15C5 complexes Cu^+ within the buried CZTS, thereby inhibiting Cu^+ migration and preserving the structural integrity of $FAPbBr_3$. Additionally, 15C5 interacts with Pb^{2+} in the upper perovskite layer to passivate Pb vacancy defects and suppress carrier nonradiative recombination. This interaction enhances carrier transport and promotes radiative recombination at the HTL/perovskite interface. As a result, the optimized device achieved remarkable enhancements: peak EQE increased from 3.12% to 11.08%, L_{max} increased from 24495 to 50584 cd m^{-2}, and CE increased from 15.03 to 50.42 cd A^{-1}, corresponding to improvements of 3.5 times, 2.1 times, and 3.4 times, respectively. This study represents a significant advancement in the performance of CZTS-based PeLEDs, and provides significant implications for future optimizations of efficient and stable inorganic HTLs, thereby enhancing the prospects for high-performance optoelectronic devices.

4. Experimental Section

Materials: Lead bromide ($PbBr_2$, 99%), copper sulphate ($CuSO_4{\cdot}5H_2O$), zinc sulphate ($ZnSO_4{\cdot}7H_2O$), stannous sulfate ($SnSO_4$), sulfur powder, iso-propyl alcohol ($(CH_3)_2CHOH$), 12-crown-4 ether (12C4) (97%) and 15-crown-5 ether (15C5) (97%) were obtained from Shanghai Macklin Co, Ltd. Keshi provided ethanol, toluene (99.9%), octane (98%) and N,N-dimethylformamide (DMF, 98%). Additionally, molybdenum trioxide (MoO_3, 99.95%), oleylamine (OLA, 90%), oleic acid (OA, 90%), toluene (99.9%), nanometer nickel oxide (NiO_x, 99.5%) and LiF were sourced from Shanghai Aladdin Industrial Corporation Co., Ltd. Xi'an Polymer Light Technology Corp supplied cuprous chloride (CuCl), zinc chloride (ZnCl), stannous chloride (SnCl), formamidine bromide (FABr), 2,2',2''-(1,3,5-benzinetriyl)-tris(1-phenyl-1H-benzimidazole) (TPBi, 99.9%), and PEDOT:PSS (Clevios Al 4083).

Preparation of $FAPbBr_3$ QDs: The synthesis of $FAPbBr_3$ QDs was carried out using a modified method based on literature. The $FAPbBr_3$ precursor (150 µL), prepared by dissolving $PbBr_2$ and FABr in DMF with a molar ratio of 1:2.2 and Pb^{2+} concentration at 0.2 M, was injected into a vial containing a crystallization-inducing solution composed of 5 mL of toluene, 2 mL of 1-butanol, 500 µL of oleic acid, and 30 µL of n-diacylamine. The solution was vigorously stirred for 10 min after the injection, following which it was centrifuged at 13000 rpm for 5 min and the supernatant was discarded. The precipitate was redispersed in 1 mL of n-hexane and then centrifuged at 2000 rpm for 2 min. The resulting supernatant was filtered through a 0.22 µm PTFE filter to collect $FAPbBr_3$ QDs. Prior to the injection of the precursor, the crystallization-inducing solution was precooled to 8–10 °C.

Preparation of CZTS Films: The colloidal CZTS nanocrystals were synthesized using the hot injection method. A mixture of 0.15 M copper sulfate ($CuSO_4{\cdot}5H_2O$), 0.075 M zinc sulphate ($ZnSO_4{\cdot}7H_2O$), 0.075 M stannous sulphate ($SnSO_4$), and 10 mL of oleylamine (OLA) was prepared in a three-neck flask at room temperature. The resulting solution was stirred constantly and heated to 130 °C for 40 min. Then, the reaction temperature was raised to 240 °C before rapidly injecting 5 mL of the previously prepared sulfur precursor solution (3 M) into the preheated Cu-Zn-Sn-OLA complex solution. After half an hour the reaction was complete and which were purified once time. CZTS ink (40 mg mL^{-1}) was obtained by dissolved in toluene solvent, then CZTS ink was added to 12-crown-4 ether (12C4) or 15-crown-5 ether (15C5) (volume ratio 10:1) and stirred overnight to form a mixture of CZTS and 12C4 or 15C5. CZTS without 15C5 and 12C4 (W/O CZTS) film were obtained by spinning CZTS ink on the ITO substrate. 12C4 (15C5) CZTS film were obtained by spinning mixture of CZTS and 12C4 (15C5) on the ITO substrate. Pure 15C5 film were obtained by spinning mixture of 15C5 on the ITO substrate.

Device Fabrication: $FAPbBr_3$ QDs were spin-coated at 1000 rpm for 60 s on the CZTS films and then quickly transferred into a high-vacuum evaporator without annealing. Afterward, in a low-vacuum environment of 8×10^{-5} Pa, a sequential deposition of 50 nm TPBi, 1 nm of LiF, and 80 nm of Al was carried out. The hole-only device was fabricated by sequentially deposit a 3 nm of MoO_3 and 80 nm of Ag onto perovskite film.

Characterizations: The crystalline structure and quality of the CZTS nanocrystal films were investigated by X-ray diffraction (XRD; X'Pert ProX-ray diffractometer) employing a Cu Kα (λ = 1.5418 Å) and Raman spectroscopy (Renishaw) using an Argon-ion laser (wavelength of 514.5 nm) at room temperature. The Raman spectra were acquired at constant incident laser power of 2.5 mW. A JEOL JSM-7800 Prime scanning electron microscopy (SEM) with an accelerating voltage of 5 kV and atomic force microscopy (AFM, Bruker NanoScope V) with peak force tapping mode using silicon tips (TESP, Veeco) were used to characterize the morphologies of the films. The UV absorption spectra was obtained by UV-2500 (Shimadzu corporation). The PL spectra, TRPL spectra, and temperature-dependent photoluminescence spectra were investigated using FLS980 (Edinburgh Instruments) spectrometer with a 450 W Xenon lamp. The room-temperature absolute PLQY of the films were measured on Edinburgh-FLS 980 spectrometer by an integrating sphere. Fourier transform infrared (FTIR) spectroscopy patterns were obtained to determine the types and changes of functional groups in materials using a TENSOR II spectrometer (Bruker) with a spectral resolution of 4 cm^{-1} at a scanning frequency of 1 spectra min^{-1}. The characterizations of low-(f = 5 K) and high-frequency (f = 100 K) capacitance–voltage curves of PeLEDs were performed by Keithley 4200. The Keithley 2400 source meter combined with a QE-Pro spectrometer (Ocean Optics), were employed to characterize the performances of PeLEDs in glove box. The intensity of electroluminescence was measured by a FOIS-1 integration sphere.

Supporting Information

Supporting Information is available from the Wiley Online Library or from the author.

Acknowledgements

This work was supported by the National Natural Science Foundation of China (No. 52202188 and No. 11704050), and Supported by the Joint Innovation Fund Project of Lanzhou Jiaotong University and Southwest Jiaotong University Supporting. The authors thank the Analysis and Testing Center of Southwest Jiaotong University for supporting the XRD measurements.

Conflict of Interest

The authors declare no conflict of interest.

Data Availability Statement

The data that support the findings of this study are available from the corresponding author upon reasonable request.

Keywords

Cu_2ZnSnS_4, inorganic hole transport layer, ion migration, perovskite light-emitting diodes

Received: July 4, 2024
Revised: August 22, 2024
Published online: September 6, 2024

[1] J. Jiang, Z. Chu, Z. Yin, J. Li, Y. Yang, J. Chen, J. Wu, J. You, X. Zhang, *Adv. Mater.* **2022**, *34*, 2204460.
[2] S. Yuan, L. Dai, Y. Sun, F. Auras, Y. H. Zhou, R. Z. An, Y. Liu, C. Ding, C. Cassidy, X. Tang, S. C. Dong, H. B. Kang, K. Chen, X. Liu, Z. F. Ye, Y. Zhao, C. Adachi, L. S. Liao, N. C. Greenham, Y. Qi, S. D. Stranks, L. S. Cui, R. H. Friend, *Nat. Photonics* **2024**, *18*, 425.
[3] S. Ding, Q. Wang, W. Gu, Z. Tang, B. Zhang, C. Wu, X. Zhang, H. Chen, X. Zhang, R. Cao, *Nat. Photonics* **2024**, *18*, 363.
[4] S. Q. Sun, J. W. Tai, W. He, Y. J. Yu, Z. Q. Feng, Q. Sun, K. N. Tong, K. Shi, B. C. Liu, M. Zhu, *Adv. Mater.* **2024**, *36*, 2400421.
[5] Q. Zhang, Y. Zhao, X. Qin, M. Li, H. Sun, P. Zhou, W. Feng, Y. Li, J. Lu, K. Lin, *Adv. Funct. Mater.* **2024**, *34*, 2308547.
[6] B. R. Lee, J. w. Kim, D. Kang, D. W. Lee, S. J. Ko, H. J. Lee, C. L. Lee, J. Y. Kim, H. S. Shin, M. H. Song, *ACS Nano* **2012**, *6*, 2984.
[7] J. M. Yun, J. S. Yeo, J. Kim, H. G. Jeong, D. Y. Kim, Y. J. Noh, S. S. Kim, B. C. Ku, S. I. Na, *Adv. Mater.* **2011**, *23*, 4923.
[8] H. Choi, C.-K. Mai, H. B. Kim, J. Jeong, S. Song, G. C. Bazan, J. Y. Kim, A. J. Heeger, *Nat. Commun.* **2015**, *6*, 7348.
[9] A. G. Ricciardulli, S. Yang, N. B. Kotadiya, G. J. A. H. Wetzelaer, X. Feng, P. W. M. Blom, *Adv. Electron. Mater.* **2019**, *5*, 1800687.
[10] J. You, L. Meng, T. B. Song, T. F. Guo, Y. Yang, W. H. Chang, Z. Hong, H. Chen, H. Zhou, Q. Chen, *Nat. Nanotechnol.* **2016**, *11*, 75.
[11] R. Chakraborty, H. Bhunia, S. Chatterjee, A. J. Pal, *J. Solid State Chem.* **2020**, *281*, 121021.
[12] Y. L. Shi, M.-P. Zhuo, X. C. Fang, X. Q. Zhou, X. D. Wang, W. F. Chen, L. S. Liao, *J. Phys. Chem. Lett.* **2020**, *11*, 7624.
[13] S. Zhuang, J. He, X. Ma, Y. Zhao, H. Wang, B. Zhang, *Mater. Sci. Semicond. Process.* **2020**, *109*, 104924.
[14] X. Cui, Y. Li, Z. Chen, Y. Zou, Y. Liu, B. Sun, Z. Bo, *J. Alloys Compd.* **2023**, *960*, 170823.
[15] L. Zhang, F. Yuan, J. Xi, B. Jiao, H. Dong, J. Li, Z. Wu, *Adv. Funct. Mater.* **2020**, *30*, 2001834.
[16] B. Chen, H. Chen, Y. Hou, J. Xu, S. Teale, K. Bertens, H. Chen, A. Proppe, Q. Zhou, D. Yu, *Adv. Mater.* **2021**, *33*, 2103394.
[17] Y. Wu, Z. Xiao, Y. Lian, L. He, X. Yang, Q. Wang, J. Ren, G. Li, X. Yang, *Org. Electron.* **2019**, *75*, 105420.
[18] C. Yi, A. Wang, C. Cao, Z. Kuang, X. Tao, Z. Wang, F. Zhou, G. Zhang, Z. Liu, H. Huang, *Adv. Mater.* **2024**, *36*, 2400658.
[19] Q. Zhang, D. Zhang, B. Cao, S. Poddar, X. Mo, Z. Fan, *ACS Nano* **2024**, *18*, 8557.
[20] T. J. Huang, X. Yin, C. Tang, G. Qi, H. Gong, *J. Mater. Chem. A* **2015**, *3*, 17788.
[21] B. R. Bade, S. R. Rondiya, Y. A. Jadhav, M. M. Kamble, S. V. Barma, S. B. Jathar, M. P. Nasane, S. R. Jadkar, A. M. Funde, N. Y. Dzade, *J. Alloys Compd.* **2021**, *854*, 157093.
[22] K. W. Huang, M. H. Li, P. T. Hsieh, C. F. Lin, R. Rajendran, Y. L. Tung, P. Chen, *J. Mater. Chem. C* **2022**, *10*, 16016.
[23] L. Song, L. Huang, Y. Hu, X. Guo, X. Liu, C. Geng, S. Xu, N. Luan, W. Bi, L. Wang, *J. Mater. Chem. C* **2020**, *8*, 9986.
[24] Y. Han, Z. Meng, Y. X. Ma, C. F. Chen, *Acc. Chem. Res.* **2014**, *47*, 2026.
[25] J. W. Steed, *Coord. Chem. Rev.* **2001**, *215*, 171.
[26] G. J. Lumetta, B. A. Moyer, *J. Coord. Chem.* **1990**, *22*, 331.
[27] S. J. Kim, Y. Kim, R. K. Chitumalla, G. Ham, T. D. Nguyen, J. Jang, H. Cha, J. Milić, J. H. Yum, K. Sivula, *J Energy Chem* **2024**, *92*, 263.
[28] Y. Liu, X. Shen, Q. Xian, H. Chen, H. Zou, S. Gao, *J. Hazard. Mater.* **2006**, *137*, 1149.
[29] M. Banerjee, A. Gupta, S. K. Saha, D. Chakravorty, *Small* **2015**, *11*, 3451.
[30] Y. Inokuchi, T. Ebata, T. Ikeda, T. Haino, T. Kimura, H. Guo, Y. Furutani, *New J. Chem.* **2015**, *39*, 8673.
[31] S. A. Veldhuis, Y. F. Ng, R. Ahmad, A. Bruno, N. F. Jamaludin, B. Damodaran, N. Mathews, S. G. Mhaisalkar, *ACS Energy Lett.* **2018**, *3*, 526.
[32] Y. Sui, W. Zhou, D. Khan, S. Wang, T. Zhang, G. Yu, Y. Huang, X. Yang, K. Chang, Y. He, *ACS Energy Lett.* **2024**, *9*, 1518.
[33] T. S. Su, F. T. Eickemeyer, M. A. Hope, F. Jahanbakhshi, M. Mladenovic, J. Li, Z. Zhou, A. Mishra, J. H. Yum, D. Ren, *J. Am. Chem. Soc.* **2020**, *142*, 19980.
[34] Y. Yang, T. Zhao, M. H. Li, X. Wu, M. Han, S. C. Yang, Q. Xu, L. Xian, X. Chi, N. J. Zhao, *Chem. Eng. J.* **2023**, *451*, 138962.
[35] J. Zhang, S. Yang, W. Liu, Q. Xue, *Wear* **1999**, *236*, 303.
[36] B. Ai, C. Liu, Z. Deng, J. Wang, J. Han, X. Zhao, *Phys. Chem. Chem. Phys.* **2017**, *19*, 17349.
[37] T. J. Savenije, C. S. Ponseca Jr, L. Kunneman, M. Abdellah, K. Zheng, Y. Tian, Q. Zhu, S. E. Canton, I. G. Scheblykin, T. Pullerits, *J. Phys. Chem. Lett.* **2014**, *5*, 2189.
[38] S. Wang, Y. Xie, W. Jiang, B. Liu, K. Shi, K. Pan, *Chin. Chem. Lett.* **2024**, *35*, 108521.
[39] L. Zhou, J. F. Liao, Y. Qin, X. D. Wang, J. H. Wei, M. Li, D. B. Kuang, R. He, *Adv. Funct. Mater.* **2021**, *31*, 2102654.
[40] V. M. Le Corre, E. A. Duijnstee, O. El Tambouli, J. M. Ball, H. J. Snaith, J. Lim, L. J. A Koster, *ACS Energy Lett.* **2021**, *6*, 1087.
[41] Z. Ren, J. Yu, Z. Qin, J. Wang, J. Sun, C. C. S. Chan, S. Ding, K. Wang, R. Chen, K. S. Wong, *Adv. Mater.* **2021**, *33*, 2005570.
[42] J. Cui, A. P. Beyler, I. Coropceanu, L. Cleary, T. R. Avila, Y. Chen, J. M. Cordero, S. L. Heathcote, D. K. Harris, O. Chen, *Nano Lett.* **2016**, *16*, 289.
[43] X. Zeng, C. Yan, Q. Wang, J. Cao, X. Fu, S. Yang, Y. Chen, L. Pan, W. Li, W. Yang, *Small* **2023**, *19*, 2304411.
[44] M. Ledinsky, T. Schönfeldová, J. Holovský, E. Aydin, Z. k. Hájková, L. Landová, N. Neyková, A. Fejfar, S. De Wolf, *J. Phys. Chem. Lett.* **2019**, *10*, 1368.
[45] B. Subedi, C. Li, C. Chen, D. Liu, M. M. Junda, Z. Song, Y. Yan, N. J. Podraza, *ACS Appl. Mater. Interfaces* **2022**, *14*, 7796.
[46] H. Wang, Z. Chen, F. Tian, G. Zheng, H. Wang, T. Zhang, J. Qin, X. Gao, P. A. van Aken, L. Zhang, *Adv. Energy Mater.* **2023**, *13*, 2202185.
[47] D. Shi, V. Adinolfi, R. Comin, M. Yuan, E. Alarousu, A. Buin, Y. Chen, S. Hoogland, A. Rothenberger, K. Katsiev, *Science* **2015**, *347*, 519.
[48] Z. Wu, M. Jiang, Z. Liu, A. Jamshaid, L. K. Ono, Y. Qi, *Adv. Energy Mater.* **2020**, *10*, 1903696.
[49] Q. Wang, Y. Chen, C. Yan, X. Zeng, X. Fu, L. Pan, J. Cao, S. Yang, W. Li, X. Chen, *ACS Energy Lett.* **2023**, *8*, 3710.
[50] R. Kumar, J. Kumar, P. Srivastava, D. Moghe, D. Kabra, M. Bag, *ACS Appl. Mater. Interfaces* **2020**, *12*, 34265.
[51] X. Peng, X. Yang, D. Liu, T. Zhang, Y. Yang, C. Qin, F. Wang, L. Chen, S. Li, *ACS Energy Lett.* **2021**, *6*, 4187.
[52] X. Xiao, K. Wang, T. Ye, R. Cai, Z. Ren, D. Wu, X. Qu, J. Sun, S. Ding, X. W. Sun, *Commun. Mater.* **2020**, *1*, 81.
[53] X. Xiao, T. Ye, J. Sun, X. Qu, Z. Ren, D. Wu, S. Ding, X. W. Sun, W. C. H. Choy, K. Wang, *Appl. Phys. Lett.* **2022**, *120*, 243501.
[54] Y. Chen, C. Yan, Z. Chen, X. Zeng, Q. Wang, S. Yang, L. Pan, C. Li, M. Mu, W. Li, *Mater. Today Phys.* **2024**, *43*, 101413.
[55] B. Roose, K. Dey, M. R. Fitzsimmons, Y. H. Chiang, P. J. Cameron, S. D. Stranks, *ACS Energy Lett.* **2024**, *9*, 442.
[56] F. Ebadi, N. Taghavinia, R. Mohammadpour, A. Hagfeldt, W. Tress, *Nat. Commun.* **2019**, *10*, 1574.
[57] L. S. C. Pingree, M. T. Russell, T. J. Marks, M. C. Hersam, *J. Appl. Phys.* **2006**, *100*, 044502.
[58] R. Kötz, M Carlen, *Electrochim. Acta* **2000**, *45*, 2483.
[59] C. Yan, X. Zeng, Q. Wang, X. Peng, W. Li, J. Cao, Y. Gao, X. Chu, X. Fu, S. Yang, *Nano Energy* **2022**, *102*, 107621.